MDPI

Article

Effect of Equal Channel Angular Pressing on the Microstructure and Mechanical Properties of an Mg–5Sn Alloy

Xiaoru Zhuo [1,2,3], **Cong Shao** [2], **Peng Zhang** [1], **Zhichao Hu** [1,*] **and Huan Liu** [2,4,*]

1   Nanjing Institute of Agricultural Mechanization, Ministry of Agriculture and Rural Affairs, Nanjing 210014, China
2   College of Mechanics and Materials, Hohai University, Nanjing 211100, China
3   College of Engineering, Nanjing Agricultural University, Nanjing 210031, China
4   Jiangsu Key Laboratory for Light Metal Alloys, Nanjing Yunhai Special Metals Co., Ltd., Nanjing 211200, China
*   Correspondence: huzhichao@caas.cn (Z.H.); liuhuanseu@hhu.edu.cn (H.L.)

Abstract: An Mg–5Sn alloy was processed by equal channel angular pressing (ECAP) for different passes (4P, 8P, and 12P), and the microstructure evolution and mechanical properties were investigated. The grain size, amount of Mg_2Sn precipitates, and texture of ECAP alloys depend on the number of passes. The ECAP 8P alloy has the finest grains and largest area fraction of Mg_2Sn particles, followed by the ECAP 12P alloy. The ECAP 4P and 8P alloys exhibit basal textures tilted towards transverse direction (TD), whereas the ECAP 12P alloy shows basal texture with the *c*-axis of the grains parallel to the extrusion direction (ED). ECAP alloys show superior strengths compared to the as-cast alloy, mainly attributed to fine grain strengthening, precipitation strengthening, texture strengthening, and dislocation strengthening. The ultimate tensile strength (UTS) increases while the elongation (EL) decreases with increasing ECAP pass.

Keywords: Mg–Sn alloy; equal channel angular pressing; strength; ductility

check for updates

1. Introduction

The crises of global warming, environmental deterioration, and resource shortage drive the growing demand for light-weight materials [1,2]. Mg alloys are potential light-weight structural materials for applications in various industrial sectors such as rail traffic, automobiles, and aircraft due to their high specific strength, excellent damping capacity, and good castability [3–5]. However, the development of high-performance Mg alloys has heavily relied on rare earth (RE) elements [6,7]. The addition of RE elements boosts the cost of Mg alloys, severely limiting their application. Therefore, the development of RE-free Mg alloys is of huge significance.

Analogous to RE elements, Sn possesses a very high solubility in Mg at high temperatures, but a negligible solubility at room temperature. In addition, the Mg_2Sn phase has a high melting temperature of 770 °C [8]. Mg–Sn alloys are deemed as promising RE-free Mg alloys by researchers and have attracted considerable research interest over the past two decades [9–12]. Nonetheless, cast Mg–Sn alloys exhibit inferior mechanical properties. Thermomechanical processing techniques have been applied to tailor the microstructure and enhance their mechanical performance. Cheng et al. investigated the influence of hot extrusion on the microstructure and mechanical properties of Mg–xSn (x = 6, 8, 10) alloys. They reported that hot-extruded alloys exhibit enhanced yield strength (YS), mainly due to grain refinement and the presence of fine Mg_2Sn precipitates [12,13]. Zhao et al. found that the YS and UTS of hot-extruded Mg–xSn (x = 1, 3, 5, 7) alloys increase, but EL decreases with increasing Sn content [14]. The strain hardening ability of hot-extruded Mg–Sn alloys also decreases with increasing Sn content [15]. A hot-extruded Mg–5Sn alloy processed by

coupling twinning, aging, and detwinning (TAD) exhibits higher strength compared to its counterpart without TAD [16].

ECAP is an effective severe plastic deformation (SPD) technique to improve the mechanical properties of metallic materials. ECAP has been broadly employed to process Mg alloys [17–20]. However, surprisingly, the effect of ECAP on the mechanical performance of Mg–Sn alloys has rarely been reported. In this work, the influence of ECAP on the microstructure and mechanical properties of an Mg–5Sn alloy was examined. The results presented in this work may provide guidance for the development of high-performance Mg–Sn alloys.

2. Materials and Methods

To fabricate the targeted Mg–5Sn (in weight percent, wt.%) alloy, pure Mg (99.9%) and pure Sn (99.99%) ingots were melted in a graphite crucible placed in an electric resistance furnace (Nanjing, China) and then cast in a steel mold pre-heated to 300 °C, under CO_2 (99% in volume) and SF_6 (1% in volume) mixed atmosphere. The crucible and mold were coated with zirconia before being used. To dissolve intermetallic phases in Mg–5Sn ingots, solid solution treatment was conducted at 480 °C for 12 h, followed by water quenching. Subsequently, Mg–5Sn ingots were cut into small pieces with a dimension of 20 mm × 20 mm × 45 mm by wire electrical discharge machining, which were then ECAP processed for 4, 8, and 12 passes at 390 °C. The corresponding processed ECAP pieces are denoted by ECAP 4P, ECAP 8P, and ECAP 12P alloys, respectively.

Room temperature tensile tests were performed with a CMT5105 electronic universal testing machine(Tianjin, China) with a loading rate of 0.5 mm/s. Tensile test specimens are dog-bone-shaped with a gauge size of 2 mm × 2 mm × 7 mm, as shown in Figure 1. At least 3 samples were tested for each alloy state to render reliable results. For ECAP alloys, the tensile direction is along ED. Microstructures of specimens were characterized by X-ray diffraction (XRD, Bruker D8 DISCOVER, Bruker, MA, USA), optical microscopy (OM, Olympus BX51M, Olympus, Tokyo, Japan), and scanning electron microscopy (SEM, ZEISS G300, Zeiss, Oberkochen, Germany) equipped with electron backscatter diffractions system (EBSD) and energy dispersive spectroscopy (EDS). OM, SEM, and EBSD specimens were prepared following the procedure described in [19]. The average size and area fraction of particles in ECAP alloys were obtained with the Image-Pro Plus. EBSD data were post-processed with the Channel 5 software. All EBSD results presented in this work were obtained by using this software.
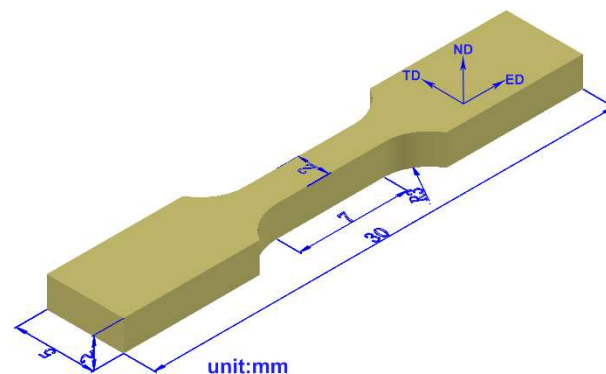

Figure 1. Schematic diagram of the tensile test specimen.

3. Results and Discussion

3.1. Microstructure Evolution

Figure 2 exhibits OM and SEM microstructures of as-cast and solid-solution-treated (SS) Mg–5Sn alloys. It can be noted that the as-cast Mg–5Sn alloy consists of an α–Mg matrix and intermetallic compounds. High-resolution images showing the intermetallic phase are presented in Figure 2 as insets. EDS was conducted to determine the composition

of the intermetallic phase, the results of which are shown in Figure 3. The intermetallic phase was identified to be the Mg_2Sn phase. XRD analysis shown in Figure 4 confirms that the as-cast Mg–5Sn alloy is composed of α–Mg and Mg_2Sn phases. Mg_2Sn particles in the as-cast alloy are very coarse and plate-like, with a size of around tens of microns. Mg_2Sn particles were mostly dissolved by solid solution treatment, but a few of them remained near grain boundaries (Figure 2), consistent with previous studies [11,21]. The remaining Mg_2Sn particles are smaller than that in the as-cast alloy. The peak for the Mg_2Sn phase cannot be observed from the XRD results for the SS alloy shown in Figure 4. This is because of the tiny amount of Mg_2Sn phase remaining in the SS alloy.
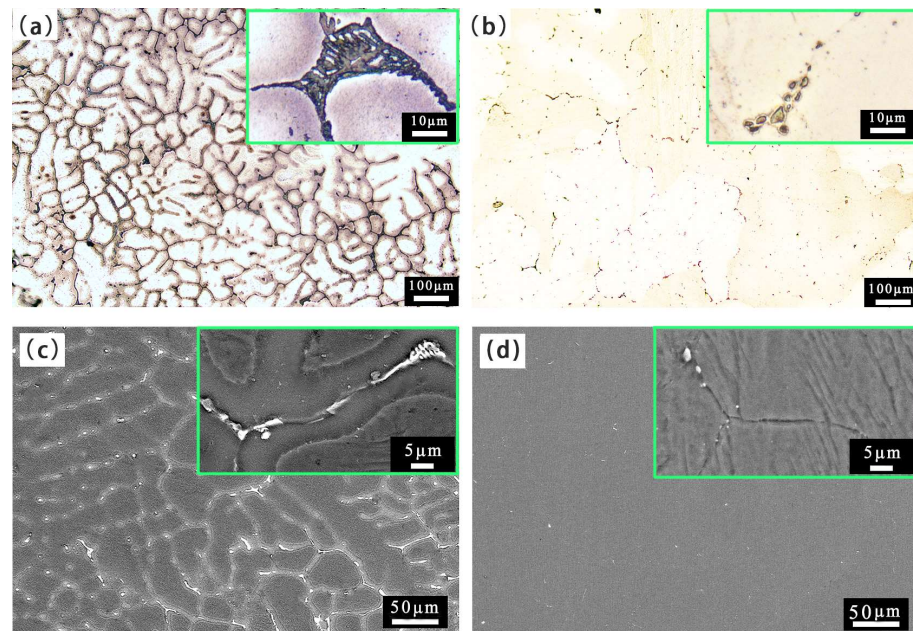

Figure 2. OM (**a**,**b**) and SEM (**c**,**d**) images of as-cast (**a**,**c**) and solid-solution-treated (**b**,**d**) Mg–5Sn alloys. Insets are high-resolution images showing the intermetallic phase.
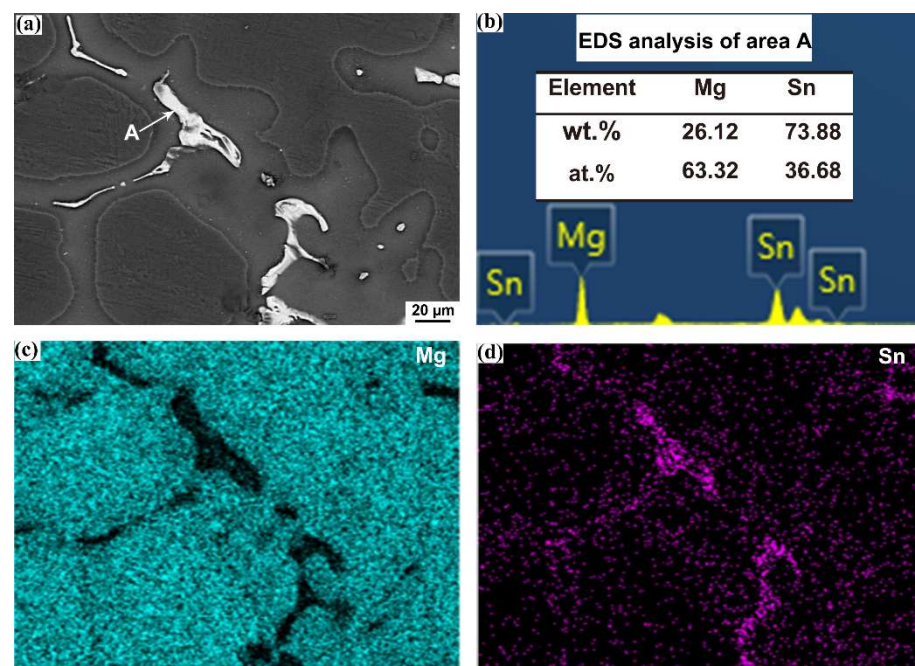

Figure 3. (**a**) SEM image showing intermetallic particles in the as-cast Mg–5Sn alloy, (**b**) EDS analysis of area A, and (**c**,**d**) EDS mapping of the region shown in (**a**).
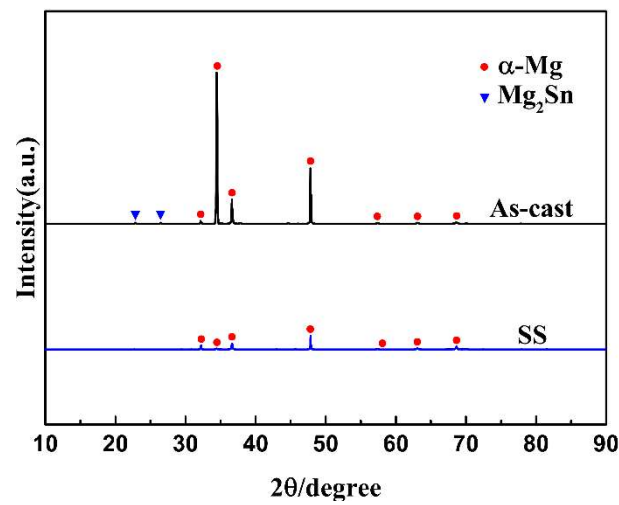
Figure 4. XRD pattern of the as-cast and SS Mg–5Sn alloy.

Figure 5 shows SEM micrographs of the ECAP alloys. Noticeably, numerous fine Mg_2Sn precipitates exist in the ECAP alloys. They were mainly generated during ECAP by dynamic precipitation. Plastic deformation inducing dynamic precipitation is a common phenomenon in Mg–Sn-based alloys, which are aging-hardenable, as extensively reported by previous studies [11,14,22,23]. In addition, some coarse and blocky Mg_2Sn particles can be observed. Recalling that a few coarse Mg_2Sn particles were undissolved after solid solution treatment, it is obvious that these undissolved particles were fragmentized by ECAP and changed to be blocky-shaped. ECAP inducing the fragmentation of second-phase particles was also observed by other studies [24].
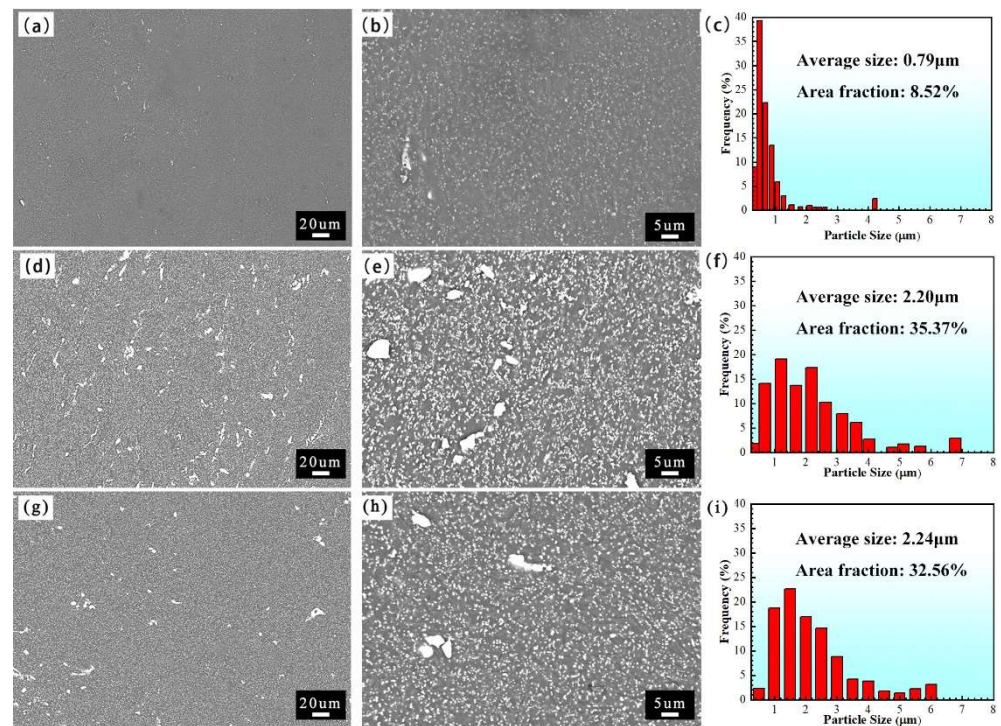
Figure 5. SEM images of (**a**,**b**) ECAP 4P alloy, (**d**,**e**) ECAP 8P alloy, and (**g**,**h**) ECAP 12P alloy. Statistics of Mg_2Sn particles in (**c**) ECAP 4P alloy, (**f**) ECAP 8P alloy, and (**i**) ECAP 12P alloy.

Interestingly, the size and amount of Mg_2Sn particles depend on the extent of deformation. Specifically, as ECAP passes increase from 4P to 8P, the average size and area fraction

of the Mg_2Sn particles increase from 0.79 µm and 8.52% to 2.20 µm and 35.57%, respectively. With the further increase in ECAP passes to 12P, the change in the average size is negligible, but the area fraction reduces slightly to 32.56%. This phenomenon can be rationalized by considering the competition between dynamic precipitation and dissolution of the Mg_2Sn phase. Dynamic precipitation is closely related to dislocations which are potential nucleation sites for Mg_2Sn precipitates [25]. Dissolution of the Mg_2Sn phase depends on temperature, and higher temperatures promote dissolution. In the early stage of ECAP, the dislocation density is relatively low and dynamic precipitation is in an early stage. Therefore, Mg_2Sn precipitates in the ECAP 4P alloy are very fine, and their distribution is sparse. As ECAP passes increase to 8P, more dislocations were accumulated in the alloy, providing more nucleation sites. Moreover, Mg_2Sn precipitates precipitated in the early stage provide additional nucleation sites. Consequently, the sizes of the Mg_2Sn precipitates in ECAP 8P are larger than that in the ECAP 4P alloy, and their area fraction rises sharply to 35.57%. In other words, in the cases of the ECAP 4P and 8P alloys, dynamic precipitation is dominant over dissolution of the Mg_2Sn phase because of the abundance of Sn solute atoms in the Mg matrix and relatively low temperature. In contrast, with the further increase in ECAP passes to 12P, the actual temperature of the deformation zone is relatively high due to the heat produced by plastic deformation and friction during ECAP [26–28]. Meanwhile, Sn solute atoms in the Mg matrix may have been depleted after ECAP 8P. Therefore, in the case of the ECAP 12P alloy, dissolution of the Mg_2Sn phase is dominant over dynamic precipitation due to the relatively high temperature and depletion of Sn solute atoms. The area fraction of Mg_2Sn precipitates decreases slightly.

Inverse pole figure (IPF) maps and grain size distribution of ECAP alloys are shown in Figure 6. Grains are colored by orientation according to the color code (shown as the inset in Figure 6). Compared to the as-cast alloy, ECAP alloys show significantly refined grains, with an average grain size (AGS) of 3–5 µm. Grain refinement is due to dynamic recrystallization (DRX) during ECAP. Interestingly, AGS decreases from 4.61 to 3.03 µm as ECAP pass increases from 4P to 8P but increases to 3.95 µm with the further increase in ECAP pass to 12P. The grain growth is due to the high deformation temperature (390 °C) and the heat generated during ECAP.

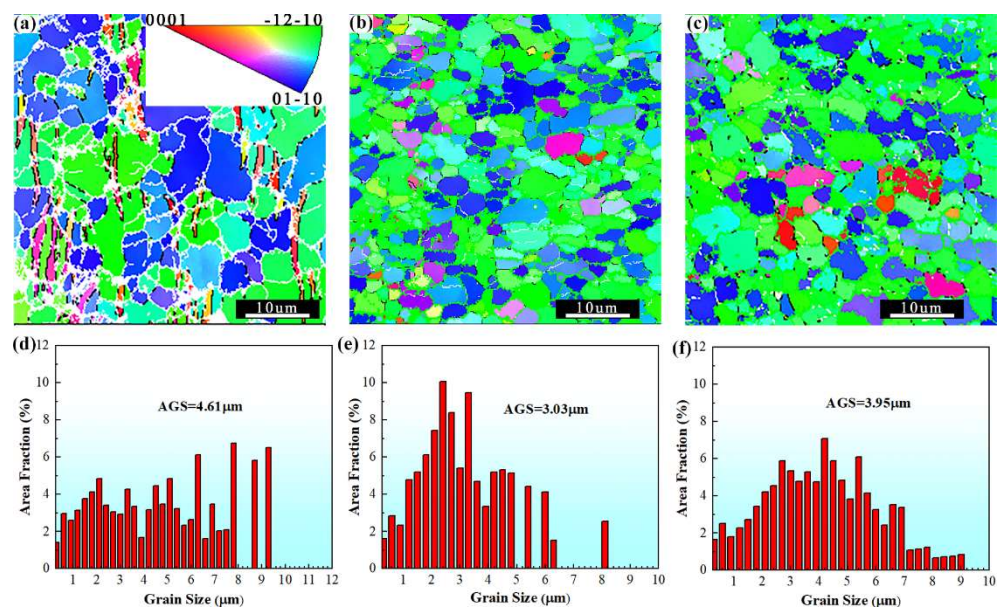**Figure 6.** IPF maps of (**a**) ECAP 4P alloy, (**b**) ECAP 8P alloy, and (**c**) ECAP 12P alloy. Statistics of grains in (**d**) ECAP 4P alloy, (**e**) ECAP 8P alloy, and (**f**) ECAP 12P alloy.

Figure 7 exhibits pole figures of ECAP alloys. It can be noted that all ECAP alloys have basal textures, but the orientations of the *c*-axes are different. The *c*-axes of the grains

in the ECAP 4P and 8P alloys are mostly tilted towards TD, away from ED. In contrast, the *c*-axis of the grains in the ECAP 12P alloy is parallel to ED. In addition, texture intensities of the three alloys are different. The ECAP 4P alloy has the strongest texture intensity of 50.38, while the ECAP 8P alloy possesses the weakest texture intensity of 18.76. It has been reported that unDRXed grains have a stronger basal texture than DRXed grains [26,29,30]. Thus, it is speculated that the variation in texture intensity is related to the change in the fraction of unDRXed grains. Figure 8 shows different types of grains and their fractions in ECAP alloys. The ECAP 4P alloy has the largest frequency of unDRXed grains, followed by the ECAP 12P alloy. The variation in the frequency of unDRXed grains with ECAP passes is consistent with that of texture intensity.
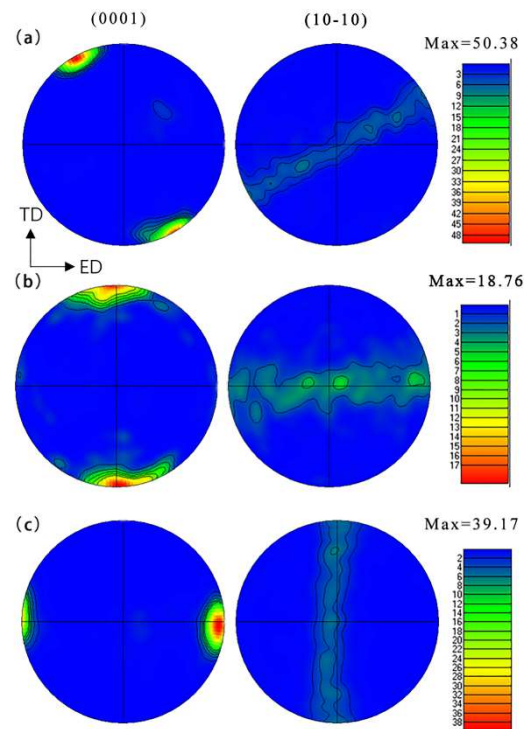

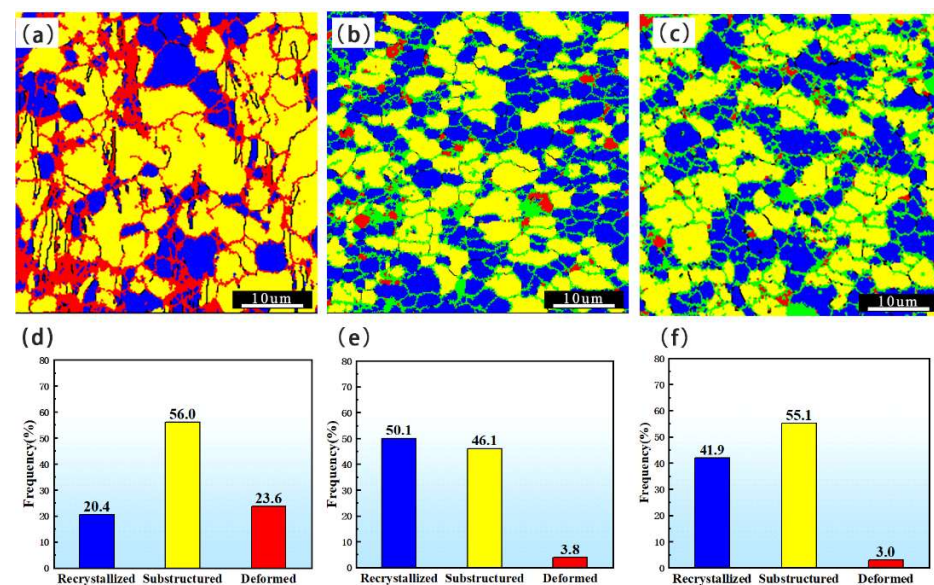**Figure 7.** Pole figures on the TD–ED cross-section of (**a**) ECAP 4P alloy, (**b**) ECAP 8P alloy, and (**c**) ECAP 12P alloy.

Figure 8. Different types of grains and their frequencies in (**a**,**d**) ECAP 4P alloy, (**b**,**e**) ECAP 8P alloy, and (**c**,**f**) ECAP 12P alloy.

Figure 9 shows kernel average misorientation (KAM) maps of ECAP alloys. The ECAP 8P alloy has the lowest average KAM value of 0.363, while the ECAP 8P alloy has the largest average KAM value of 0.389. KAM value can be regarded as an indication of dislocation density in alloys. A higher KAM value indicates a higher dislocation density [19]. DRX consumes dislocations and can thus lead to a reduction in dislocation density. The lowest KAM value of the ECAP 8P alloy is associated with its highest frequency of DRXed grains.
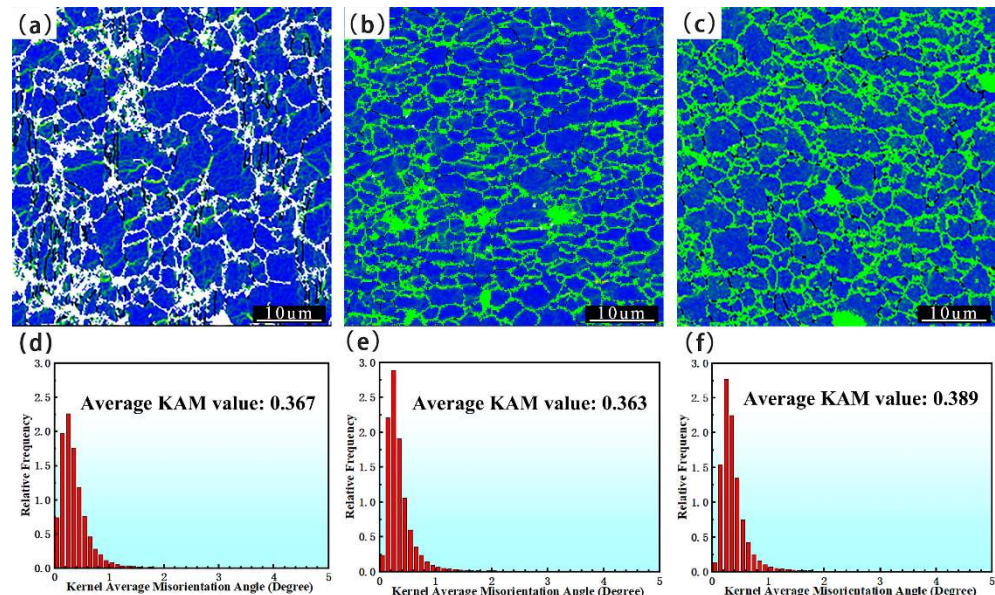

Figure 9. KAM maps and KAM distributions in (**a**,**d**) ECAP 4P alloy, (**b**,**e**) ECAP 8P alloy, and (**c**,**f**) ECAP 12P alloy.

3.2. Mechanical Properties

Figure 10 exhibits typical engineering stress–strain curves of as-cast, SS, and ECAP alloys. The yield strength (YS), ultimate tensile strength (UTS), and elongation (EL) of these alloys are summarized in Table 1. ECAP alloys possess significantly enhanced strength compared to the as-cast alloy. The strength enhancement is mainly attributed to grain refinement strengthening, precipitation strengthening, dislocation strengthening, and texture strengthening. As ECAP passes increase from 4P to 12P, the UTS increases continuously from 208 to 275 MPa. The SS alloy has the best ductility due to the absence of coarse Mg_2Sn particles and dislocations.
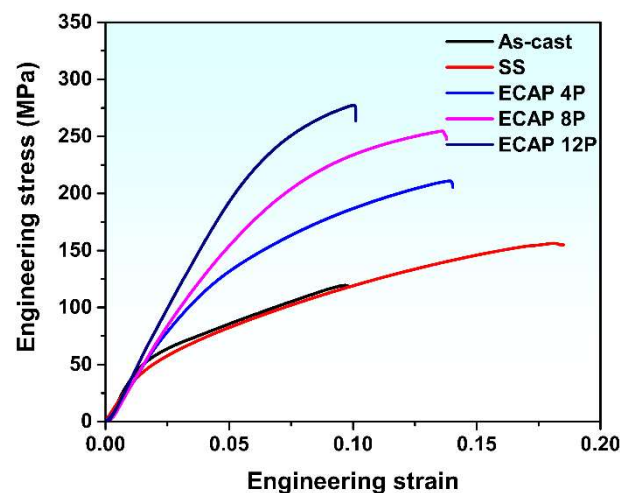

Figure 10. Typical engineering stress–strain curves of as-cast, SS, and ECAP alloys.

Table 1. Summary of mechanical properties of as-cast, SS, and ECAP alloys.

Alloys	YS (MPa)	UTS (MPa)	EL (%)
As-cast alloy	49 ± 5	133 ± 8	9.8 ± 2.1
SS alloy	44 ± 2	156 ± 6	18.5 ± 1.3
ECAP 4P alloy	82 ± 4	208 ± 2	14.0 ± 1.4
ECAP 8P alloy	94 ± 3	256 ± 3	13.8 ± 1.8
ECAP 12P alloy	115 ± 4	275 ± 5	10.1 ± 0.5

To explain the variation in strength with ECAP passes, we need to recall the microstructure evolution during ECAP. Compared to the ECAP 4P alloy, the ECAP 8P alloy has finer grains, much higher area fraction of Mg_2Sn precipitates, and almost the same KAM value but lower texture tensity. Fine grain strengthening and precipitation strengthening are stronger, but texture strengthening is weaker in the ECAP 8P alloy than in the ECAP 4P alloy. The higher UTS in the ECAP 8P alloy indicates that the increase in fine grain strengthening and precipitation strengthening is larger than the reduction in texture strengthening. In comparison with the ECAP 8P alloy, the ECAP 12P alloy possesses larger grains, slightly lower area fraction of Mg_2Sn precipitates, higher KAM value, and much stronger texture intensity, induing weaker fine grain strengthening and precipitation strengthening, but stronger dislocation strengthening and texture strengthening. The higher UTS in the ECAP 12P alloy implies that the increase in dislocation strengthening and texture strengthening is higher than the reduction in fine grain strengthening and precipitation strengthening.

In contrast to UTS, EL shows a descending trend with the increase in ECAP passes. Ductility is related to grain size, texture, dislocation density, and precipitates. Larger grains provide more room for dislocation storage than finer grains and thus are good for ductility [31,32]. Strong basal texture along the tensile direction is detrimental to ductility [31,33–37]. Dislocations [32,35] and precipitates [38,39] of high density can inhibit dislocation movements and thus promote stress concentration, deteriorating the ductility of alloys. Among all ECAP alloys, the ECAP 4P alloy has relatively large grains, low dislocation density, low area fraction of Mg_2Sn precipitates, and tilted basal texture, leading to its largest EL. Compared to the ECAP 4P alloy, the ECAP 8P alloy has finer grains and much more Mg_2Sn precipitates. Therefore, the ECAP 8P alloy exhibits poorer ductility than the ECAP 4P alloy. Although the ECAP 12P alloy possesses slightly larger grains and slightly less Mg_2Sn precipitates than the ECAP 8P alloy, it has a larger dislocation density. More importantly, the ECAP 12P alloy is featured by strong basal texture with the *c*-axis of the grains parallel to the ED. Thus, it has a lower EL than the ECAP 8P alloy.

4. Conclusions

The effect of ECAP on the microstructure and mechanical properties of an Mg–5Sn alloy was investigated. Compared to the as-cast alloy, ECAP alloys show significantly refined grains. The ECAP 8P alloy has the smallest average grain size of 3.03 μm, followed by the ECAP 12P alloy with an average grain size of 3.95 μm. As ECAP pass increases from 4P to 8P, the area fraction of Mg_2Sn precipitates rises from 8.52% to 35.57%, but decreases to 32.56% with the further increase in ECAP passes to 12P. The ECAP 4P and 8P alloys have basal textures tilted towards TD, while the ECAP 12P alloy shows a basal texture with the *c*-axis of the grains parallel to ED. The ECAP alloys possess significantly enhanced strengths compared to the as-cast alloy, mainly due to fine grain strengthening, precipitation strengthening, texture strengthening, and dislocation strengthening. UTS shows an increasing trend with increasing ECAP pass, whereas EL exhibits a decreasing trend.

Author Contributions: Conceptualization, X.Z., H.L. and Z.H.; Investigation, X.Z., C.S. and P.Z.; Writing—original draft preparation, X.Z.; Writing—review and editing, H.L. and Z.H.; Supervision, Z.H. All authors have read and agreed to the published version of the manuscript.

Data Availability Statement: The data that support the findings of this study are available from the corresponding author on request.

Conflicts of Interest: The authors declare no conflict of interest.

References

1. Wang, Y.; Liu, B.; Zhao, X.a.; Zhang, X.; Miao, Y.; Yang, N.; Yang, B.; Zhang, L.; Kuang, W.; Li, J.; et al. Turning a native or corroded Mg alloy surface into an anti-corrosion coating in excited CO_2. *Nat. Commun.* **2018**, *9*, 4058. [CrossRef] [PubMed]
2. Zhuo, X.; Zhang, Q.; Liu, H.; Hu, Z.; Zhang, P.; Jiang, J.; Ma, A.; Wu, Y. Enhanced tensile strength and ductility of an Al-6Si-3Cu alloy processed by room temperature rolling. *J. Alloy Compd.* **2022**, *899*, 163321. [CrossRef]
3. Yu, H.; Ren, J.; Kang, S.; Yu, W.; Wang, Z.; Feng, J.; Wang, Q.; Ji, P.; Zhang, X.; Yin, F. Effect of 1wt%Zn addition on microstructure and mechanical properties of Mg-6Er alloys under high strain rates. *Metals* **2022**, *12*, 883. [CrossRef]
4. Xu, T.; Yang, Y.; Peng, X.; Song, J.; Pan, F. Overview of advancement and development trend on magnesium alloy. *J. Magnes. Alloy* **2019**, *7*, 536–544. [CrossRef]
5. Zhuo, X.R.; Ma, A. Molecular dynamics-based cohesive zone model for Mg/Mg(17)Al(12) interface. *Metals* **2020**, *10*, 836. [CrossRef]
6. Yang, Y.; Xiong, X.; Chen, J.; Peng, X.; Chen, D.; Pan, F. Research advances in magnesium and magnesium alloys worldwide in 2020. *J. Magnes. Alloy* **2021**, *9*, 705–747. [CrossRef]
7. Prasad, S.V.S.; Prasad, S.B.; Verma, K.; Mishra, R.K.; Kumar, V.; Singh, S. The role and significance of Magnesium in modern day research-A review. *J. Magnes. Alloy* **2022**, *10*, 1–61. [CrossRef]
8. Nayeb-Hashemi, A.A.; Clark, J.B. *Phase Diagrams of Binary Magnesium Alloys*; ASM International: Novelty, OH, USA, 1988; 370p.
9. Pan, H.; Qin, G.; Xu, M.; Fu, H.; Ren, Y.; Pan, F.; Gao, Z.; Zhao, C.; Yang, Q.; She, J.; et al. Enhancing mechanical properties of Mg-Sn alloys by combining addition of Ca and Zn. *Mater. Des.* **2015**, *83*, 736–744. [CrossRef]
10. Pan, H.; Qin, G.; Huang, Y.; Ren, Y.; Sha, X.; Han, X.; Liu, Z.-Q.; Li, C.; Wu, X.; Chen, H.; et al. Development of low-alloyed and rare-earth-free magnesium alloys having ultra-high strength. *Acta Mater.* **2018**, *149*, 350–363. [CrossRef]
11. Cheng, W.L.; Park, S.S.; You, B.S.; Koo, B.H. Microstructure and mechanical properties of binary Mg-Sn alloys subjected to indirect extrusion. *Mater. Sci. Eng. A* **2010**, *527*, 4650–4653. [CrossRef]
12. Cheng, W.L.; Tian, Q.W.; Yu, H.; Zhang, H.; You, B.S. Strengthening mechanisms of indirect-extruded Mg–Sn based alloys at room temperature. *J. Magnes. Alloy* **2014**, *2*, 299–304. [CrossRef]
13. Cheng, W.L.; Park, S.S.; Tang, W.N.; You, B.S.; Koo, B.H. Influence of alloying elements on microstructure and microhardness of Mg-Sn-Zn-based alloys. *Trans. Nonferrous Met. Soc. China* **2010**, *20*, 2246–2252. [CrossRef]
14. Zhao, C.; Pan, F.; Zhao, S.; Pan, H.; Song, K.; Tang, A. Preparation and characterization of as-extruded Mg-Sn alloys for orthopedic applications. *Mater. Des.* **2015**, *70*, 60–67. [CrossRef]
15. Zhao, C.; Chen, X.; Pan, F.; Gao, S.; Zhao, D.; Liu, X. Effect of Sn content on strain hardening behavior of as-extruded Mg-Sn alloys. *Mater. Sci. Eng. A* **2018**, *713*, 244–252. [CrossRef]
16. Wan, Y.J.; Zeng, Y.; Zeng, Q.; Song, B.; Huang, X.F.; Qian, X.Y.; Jiang, B. Simultaneously improved strength and toughness of a Mg-Sn alloy through abundant prismatic lath-shaped precipitates. *Mater. Sci. Eng. A* **2021**, *811*, 141087. [CrossRef]
17. Liu, H.; Huang, H.; Yang, X.; Li, C.; Yan, J.; Jiang, J.; Ma, A. Microstructure and mechanical property of a high-strength Mg-10Gd-6Y-1.5Zn-0.5Zr alloy prepared by multi-pass equal channel angular pressing. *J. Magnes. Alloy* **2017**, *5*, 231–237. [CrossRef]
18. Liu, H.; Huang, H.; Zhang, Y.; Xu, Y.; Wang, C.; Sun, J.; Jiang, J.; Ma, A.; Xue, F.; Bai, J. Evolution of Mg-Zn second phases during ECAP at different processing temperatures and its impact on mechanical properties of Zn-1.6Mg (wt.%) alloys. *J. Alloy Compd.* **2019**, *811*, 151987. [CrossRef]
19. Liu, H.; Sun, C.; Wang, C.; Li, Y.; Bai, J.; Xue, F.; Ma, A.; Jiang, J. Improving toughness of a Mg2Ca-containing Mg-Al-Ca-Mn alloy via refinement and uniform dispersion of Mg2Ca particles. *J. Mater. Sci. Technol.* **2020**, *59*, 61–71. [CrossRef]
20. Xu, B.; Sun, J.; Yang, Z.; Xiao, L.; Zhou, H.; Han, J.; Liu, H.; Wu, Y.; Yuan, Y.; Zhuo, X.; et al. Microstructure and anisotropic mechanical behavior of the high-strength and ductility AZ91 Mg alloy processed by hot extrusion and multi-pass RD-ECAP. *Mater. Sci. Eng. A* **2020**, *780*, 139191. [CrossRef]
21. Chen, D.; Ren, Y.-p.; Guo, Y.; Pei, W.-l.; Zhao, H.-d.; Qin, G.-w. Microstructures and tensile properties of as-extruded Mg-Sn binary alloys. *Trans. Nonferrous Met. Soc. China* **2010**, *20*, 1321–1325. [CrossRef]
22. Tang, W.N.; Park, S.S.; You, B.S. Effect of the Zn content on the microstructure and mechanical properties of indirect-extruded Mg-5Sn-xZn alloys. *Mater. Des.* **2011**, *32*, 3537–3543. [CrossRef]

23. Sasaki, T.T.; Yamamoto, K.; Honma, T.; Kamado, S.; Hono, K. A high-strength Mg-Sn-Zn-Al alloy extruded at low temperature. *Scr. Mater.* **2008**, *59*, 1111–1114. [CrossRef]

24. Wang, C.; Ma, A.; Sun, J.; Liu, H.; Huang, H.; Yang, Z.; Jiang, J. Effect of ECAP process on as-cast and as-homogenized Mg-Al-Ca-Mn alloys with different Mg_2Ca morphologies. *J. Alloy Compd.* **2019**, *793*, 259–270. [CrossRef]

25. Ma, Y.; Han, F.-Y.; Liu, C.; Li, M.-Z. Microstructure, Texture Evolution, and Mechanical Properties of ECAP-Processed ZAT522 Magnesium Alloy. *Acta Metall. Sin. (Engl. Lett.)* **2020**, *33*, 233–242. [CrossRef]

26. Kim, H.J.; Jin, S.-C.; Jung, J.-G.; Park, S.H. Influence of undissolved second-phase particles on dynamic recrystallization behavior of Mg-7Sn-1Al-1Zn alloy during low- and high-temperature extrusions. *J. Mater. Sci. Technol.* **2021**, *71*, 87–97. [CrossRef]

27. Liu, G.; Zhou, J.; Duszczyk, J. Prediction and verification of temperature evolution as a function of ram speed during the extrusion of AZ31 alloy into a rectangular section. *J. Mater. Process. Technol.* **2007**, *186*, 191–199. [CrossRef]

28. Park, S.H.; Kim, H.S.; You, B.S. Prediction of grain size and yield strength of Mg-7Sn-1Al-1Zn alloys extruded at various temperatures and speeds. *Met. Mater. Int.* **2014**, *20*, 291–296. [CrossRef]

29. Kim, S.-H.; Lee, J.U.; Kim, Y.J.; Jung, J.-G.; Park, S.H. Controlling the microstructure and improving the tensile properties of extruded Mg-Sn-Zn alloy through Al addition. *J. Alloy Compd.* **2018**, *751*, 1–11. [CrossRef]

30. Gu, X.-j.; Cheng, W.-l.; Cheng, S.-m.; Liu, Y.-h.; Wang, Z.-f.; Yu, H.; Cui, Z.-q.; Wang, L.-f.; Wang, H.-x. Tailoring the microstructure and improving the discharge properties of dilute Mg-Sn-Mn-Ca alloy as anode for Mg-air battery through homogenization prior to extrusion. *J. Mater. Sci. Technol.* **2021**, *60*, 77–89. [CrossRef]

31. Pourbahari, B.; Mirzadeh, H.; Emamy, M.; Roumina, R. Enhanced ductility of a fine-grained Mg-Gd-Al-Zn magnesium alloy by hot extrusion. *Adv. Eng. Mater.* **2018**, *20*, 1701171. [CrossRef]

32. Zhang, Z.; Zhang, J.; Xie, J.; Liu, S.; He, Y.; Guan, K.; Wu, R. Developing a low-alloyed fine-grained Mg alloy with high strength-ductility based on dislocation evolution and grain boundary segregation. *Scr. Mater.* **2022**, *209*, 114414. [CrossRef]

33. Gao, L.; Yan, H.; Luo, J.; Luo, A.A.; Chen, R. Microstructure and mechanical properties of a high ductility Mg–Zn–Mn–Ce magnesium alloy. *J. Magnes. Alloy* **2013**, *1*, 283–291. [CrossRef]

34. Martynenko, N.S.; Lukyanova, E.A.; Serebryany, V.N.; Gorshenkov, M.V.; Shchetinin, I.V.; Raab, G.I.; Dobatkin, S.V.; Estrin, Y. Increasing strength and ductility of magnesium alloy WE43 by equal-channel angular pressing. *Mater. Sci. Eng. A* **2018**, *712*, 625–629. [CrossRef]

35. Zhang, B.P.; Geng, L.; Huang, L.J.; Zhang, X.X.; Dong, C.C. Enhanced mechanical properties in fine-grained Mg-1.0Zn-0.5Ca alloys prepared by extrusion at different temperatures. *Scr. Mater.* **2010**, *63*, 1024–1027. [CrossRef]

36. Tong, L.B.; Chu, J.H.; Sun, W.T.; Jiang, Z.H.; Zou, D.N.; Liu, S.F.; Kamado, S.; Zheng, M.Y. Development of a high-strength Mg alloy with superior ductility through a unique texture modification from equal channel angular pressing. *J. Magnes. Alloy* **2021**, *9*, 1007–1018. [CrossRef]

37. Wang, S.; Ma, J.; Yang, J.; Zhang, W.; Sun, Y.; Pan, J.; Wang, H.; Chen, W. Improving the ductility of Mg-2.5Nd-0.5Zn-0.5Zr alloy by multi-pass hot rolling. *J. Mater. Res. Technol. (JMRT)* **2021**, *14*, 2124–2130. [CrossRef]

38. Wei, X.; Jin, L.; Wang, F.; Li, J.; Ye, N.; Zhang, Z.; Dong, J. High strength and ductility Mg-8Gd-3Y-0.5Zr alloy with bimodal structure and nano-precipitates. *J. Mater. Sci. Technol.* **2020**, *44*, 19–23. [CrossRef]

39. Li, H.-z.; Liu, R.-m.; Liang, X.-p.; Deng, M.; Liao, H.-j.; Huang, L. Effect of pre-deformation on microstructures and mechanical properties of high purity Al-Cu-Mg alloy. *Trans. Nonferrous Met. Soc. China* **2016**, *26*, 1482–1490. [CrossRef]